water

MDPI

Article

Exergy Optimization of a Solar Collector in Flat Plate Shape Equipped with Elliptical Pipes Filled with Turbulent Nanofluid Flow: A Study for Thermal Management

Sara Rostami [1,2], Mohammad Sepehrirad [3], Amin Dezfulizadeh [3], Ahmed Kadhim Hussein [4], Aysan Shahsavar Goldanlou [5,6,*] and Mostafa Safdari Shadloo [7]

1 Laboratory of Magnetism and Magnetic Materials, Advanced Institute of Materials Science, Ton Duc Thang University, Ho Chi Minh City, Vietnam; sara.rostami@tdtu.edu.vn
2 Faculty of Applied Sciences, Ton Duc Thang University, Ho Chi Minh City, Vietnam
3 Department of Mechanical Engineering, Arak Branch, Islamic Azad University, Arak P.O. BOX 38135/567, Iran; m.sepehrirad97@iau-arak.ac.ir (M.S.); a.dezfulizadeh97@iau-arak.ac.ir (A.D.)
4 College of Engineering—Mechanical Engineering Department, University of Babylon, Babylon City, Hilla 51002, Iraq; ahmed.hussein.eng@uobabylon.edu.iq
5 Institute of Research and Development, Duy Tan University, Da Nang 550000, Vietnam
6 Faculty of Electrical—Electronic Engineering, Duy Tan University, Da Nang 550000, Vietnam
7 CORIA-UMR 6614, CNRS-University, INSA of Rouen and Normandie University, 76000 Rouen, France; mostafa.safdari-shadloo@insa-rouen.fr
* Correspondence: aysanshahsavargoldanlou@duytan.edu.vn

Received: 10 July 2020; Accepted: 7 August 2020; Published: 14 August 2020

Abstract: In this paper, forced convection of a multiwalled carbon nanotube (MWCNT)–water nanofluid (NF) in a new flat plate solar collector (FPSC) equipped with elliptical pipes instead of circular ones is investigated. The three-dimensional conservation equations were solved in the domain with the finite volume method (FVM) based on the semi-implicit method for pressure linked equations (SIMPLE) algorithm. The laminar-turbulent range of the Reynolds number (Re) and the volume fraction of the NF (ϕ) were 50–12,000 and 0–0.1, respectively. The optimization process was accomplished through the comparison of diverse parameters to attain the optimal case with the highest exergy efficiency. In this study, it was concluded that, in the case of using elliptical pipes instead of circular tubes, the time that the fluid was inside the FPSC increased, which led to an increase in the outlet temperature, while the exergy efficiency of the FPSC increased. Additionally, it was observed that using elliptical pipes enhanced the outlet fluid temperature, energy efficiency, and exergy efficiency. Generally, while the trend of exergy efficiency variation with effective parameters was rising, applying elliptical pipes caused the efficiency to increase. In addition, the exergy efficiency variation decreased when these parameters were changed. The highest value of exergy efficiency was 7.1%. On the other hand, for each specific FPSC, there was a unique mass flow rate at which the exergy efficiency reached its maximum value, and for higher mass flow rates, the efficiency was slightly diminished and then remained unchanged. Finally, the highest exergy efficiency was achieved for ϕ = 0.10%.

Keywords: nanofluid; flat plate solar collector; elliptical pipe; exergy optimization

1. Introduction

The use of solar energy offers numerous advantages, especially in Iran, where levels of radiation from the sun are much higher than average and where many provinces lack any centralized

infrastructure to support a national energy supply. As the demand for energy is rapidly rising in Iran, using the necessary technology to convert energy from the sun's rays into useful energy is very important for the vast majority of the population. Solar energy possesses a significantly higher potential in comparison with other renewable energies, such as wind, biomass, ocean, hydro, and geothermal sources. There are many sorts of systems that employ solar energy collectors as an input energy source in order to drive a process. Within all of these systems, the flat plate solar collector (FPSC) has a simple design and low costs of construction compared with other collector types. In addition to direct solar radiation absorption, they can also absorb diffuse radiation. The results of numerical and empirical research show that FPSC performance is dependent on a lot of factors, including pipe diameter, wind velocity, solar radiation, FPSC material, flow rate, and channel depth. However, one suitable solution to promote the efficiency of FPSCs is utilizing a heat sink below the absorber plate instead of pipes. It can augment the wetted surface between the fluid and absorber and also intensify the outlet temperature of the fluid. Furthermore, employing mixers in heat exchangers is not only one way to remove the laminar sub-layer but also a means of improving heat transfer by creating local turbulence [1–6]. The aim of this work is to examine the impact of using a heat sink and mixer on the energetic and exergetic performance of FPSCs. Another method is increasing the transmission of heat between the fluid and solar absorbing plate. One way to achieve this is through the use of nanofluids (NFs) in FPSCs. Many researchers have reported the application of NFs in thermal systems [7–13]. In this regard, Baniamerian et al. [14] employed computational fluid dynamics (CFD) to determine the aerodynamic coefficients of parabolic trough collectors. They realized that for the solar farm to operate properly, the impact of the vortices formed around the collectors by the wind must be taken into account. In another numerical investigation, Ziapour and Rahimi [15] investigated the natural convection of transmission of heat in a horizontal absorber FPSC. Their results show that as the cosine wave amplitude is enhanced, the collector enclosure irreversibility declines. Ajay and Kundan [16] conducted research on the performance assessment of NF-based parabolic solar collectors.

Previous research on FPSCs with serpentine pipes has shown that their exergy efficiency is a function of temperature and flow rate [17]. The energy efficiency relationship of FPSCs does not include these parameters. A correlation was developed by Shojaeizadeh and Veysi [18] for the exergy efficiency optimization of an H_2O-alumina NF collector. Said et al. [19] carried out an energetic and exergetic assessment of an FPSC filled with an aqueous aluminum oxide NF. In recent years, new studies have been conducted in similar fields [20–35]. Although the usage of NFs for the increased efficiency of FPSCs has been assessed, there is no study investigating the impacts of using elliptical tubes and aqueous, multiwalled carbon nanotube (MWCNT) NF-based heat sink solar collectors on the efficiency of exergy of solar collectors. Therefore, this study is expected to fill the research gap on the usage of elliptical tubes in NF-based FPSCs. The other objective of this survey is to numerically examine the impacts of ϕ on the energetic and exergetic performances of NF-cooled FPSCs using the finite volume method (FVM).

2. Methodology

2.1. Physical Model

The 3D schematic of a simulated FPSC equipped with elliptical tubes is presented in Figure 1. In addition, Table 1 shows the diverse specifications of the FPSC. For modeling, the useful energy gained by the FPSC was computed using analytical equations. Then, the useful energy received by the coolant, the leaving temperature of the coolant, and exergy efficiency were computed. The turbulent flow of the NF was assumed to be steady and incompressible. The inlet and outlet boundary conditions were uniform velocity and zero relative pressure, respectively. The Al-made absorber plate was painted black matte and exposed to a heat flux that was calculated from the empirical findings of Reference [36] for a reference FPSC (Table 2). Because the influences of overall heat loss are considered in calculating useful energy received by the FPSC, the other walls of the heat sink are assumed to be an insulator [37].

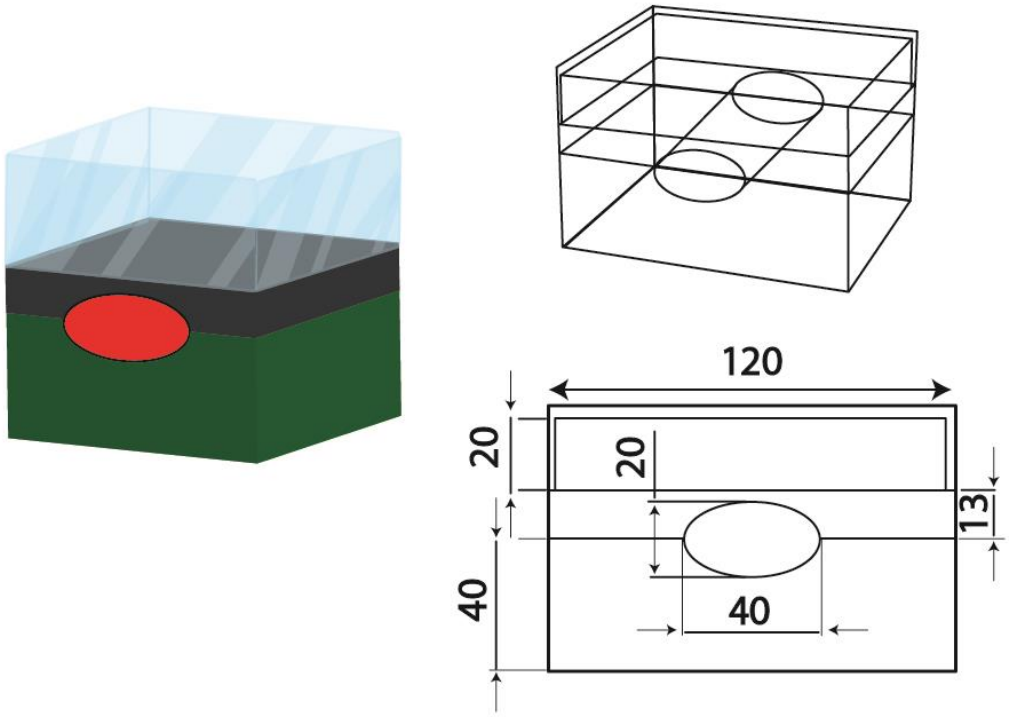

Figure 1. Schematic of the problem.

Table 1. Properties of the flat plate solar collector (FPSC) simulated in this paper.

Properties	Symbol	Quantity
Dimensions of FPSC	$L_c \times W_c$ (mm)	200 × 92.5
Slop of FPSC	β	35°
Number of glass covers	N	1
Emissivity of glass covers	ε_g	0.85
Thickness of plate	δ_p (mm)	0.1
Emissivity of plate	ε_p	0.9
Conductivity of plate	k_p (W·m^{-1}·K^{-1})	211
Optical efficiency	η_0	0.68
Thickness of insulators	δ_i (mm)	2.0
Conductivity of insulators	k_i (W·m^{-1}·K^{-1})	0.05

Table 2. Empirical results of Khorasanizadeh et al. [36] for the reference FPSC.

Time	I_T (W·m^{-2})	T_a (°C)	T_{in} (°C)	V_w (m·s^{-1})
09:00	560	33	44.5	6
09:30	630	33	45	6
10:00	750	34	46	5
10:30	830	35	47	6
11:00	925	36	50	6
11:30	992	37	51	5
12:00	1006	38	53	5
12:30	1020	38.5	54	6
13:00	978	40.5	56	6
13:30	914	40.5	57	5
14:00	834	41	60	5
14:30	780	41	61	4
15:00	734	39.5	62	5
15:30	626	41	63	6
16:00	607	41	64	6

2.2. Conservation Equations

The conservation equations used in this study are as follows:

$$\frac{\partial}{\partial x_i}(\rho u_i) = 0 \tag{1}$$

$$\frac{\partial}{\partial x_j}\left(\rho u_i u_j\right) = -\frac{\partial P}{\partial x_j} + \frac{\partial}{\partial x_j}\left[\mu\left(\frac{\partial u_i}{\partial x_j} + \frac{\partial u_j}{\partial x_i}\right)\right] + \frac{\partial}{\partial x_j}\left(-\rho\overline{u_i' u_j'}\right) \tag{2}$$

$$\frac{\partial}{\partial x_i}(\rho u_i T) = \frac{\partial}{\partial x_j}\left[\mu\left(\frac{\mu}{Pr} + \frac{\mu_t}{Pr_t}\right)\frac{\partial T}{\partial x_j}\right] \tag{3}$$

where ρ, u_i, μ, $\acute{u}$, and u_j respectively stand for the density, velocity, viscosity, fluctuated velocity, and axial velocity. In addition, $\rho\overline{u_i' u_j'}$ denotes the turbulent shear stress, which is obtained as

$$-\rho\overline{u_i' u_j'} = \mu_t\left(\frac{\partial u_i}{\partial x_j} + \frac{\partial u_j}{\partial x_i}\right) \tag{4}$$

in which μ_t denotes the turbulent viscosity, which is computed as

$$\mu_t = \rho C_\mu \frac{k^2}{\varepsilon} \tag{5}$$

where k is the turbulent kinetic energy, which is determined as

$$\frac{\partial}{\partial x_i}[\rho k u_i] = \frac{\partial}{\partial x_j}\left[\left(\mu + \frac{\mu_t}{\sigma_k}\right)\frac{\partial k}{\partial x_j}\right] + G_k - \rho\varepsilon \tag{6}$$

ε is the dissipation, which is computed as

$$\frac{\partial}{\partial x_i}[\rho\varepsilon u_i] = \frac{\partial}{\partial x_j}\left[\left(\mu + \frac{\mu_t}{\sigma_\varepsilon}\right)\frac{\partial \varepsilon}{\partial x_j}\right] + C_{1\varepsilon}\frac{\varepsilon}{k}G_k + C_{1\varepsilon}\rho\frac{\varepsilon^2}{k} \tag{7}$$

where G_k is given as

$$G_k = -\rho\overline{u_i' u_j'}\frac{\partial u_j}{\partial x_i} \tag{8}$$

where $C_\mu = 0.09$, $C_{1\varepsilon} = 1.44$, $C_{2\varepsilon} = 1.92$, $\sigma_k = 1.00$, $\sigma_\varepsilon = 1.30$, and $Pr_t = 0.90$ [38]. For all variables, 10^{-6} was considered to be the convergence criterion. The considered NF is Newtonian, and its properties are temperature dependent [39]:

$$\rho(T) = 5.3738\times10^{-10}T^5 - 9.59976\times10^{-7}T^4 + 6.93809\times10^{-4}T^3 - 0.255822T^2 + 47.8074T - 2584.53 \tag{9}$$

$$C_P(T) = -4.51782\times10^{-8}T^5 + 7.61613\times10^{-5}T^4 - 5.12699\times10^{-2}T^3 + 17.2363T^2 - 2894.85T + 198532 \tag{10}$$

$$k(T) = 5.15307\times10^{-11}T^5 - 8.15212\times10^{-8}T^4 + 5.138\times10^{-5}T^3 - 1.61344\times10^{-2}T^2 + 2.52691T - 157.532 \tag{11}$$

$$\mu(T) = -4.37087\times10^{-13}T^5 + 7.38482\times10^{-10}T^4 - 4.99292\times10^{-7}T^3 + 1.68946\times10^{-4}T^2 - 2.86313\times10^{-2}T + 1.94641 \tag{12}$$

The equation of spectral radiative transfer follows Equation (9) [40].

$$\frac{dI_v(r,s)}{ds} = -(K_{av} + K_{sv})I_v(r,s) + K_{av}I_b(v,T) + \frac{K_{sv}}{4\pi}\int_{4\pi} dI_v(r,s')\varphi(s,s')d\Omega' + S \tag{13}$$

where I_v is spectral radiation intensity, which is computed as [41]

$$I_v(r,s) = \varepsilon_v(r_w)I_b(v,T) + \frac{\rho_w(r_w)}{\pi}\int\limits_{n.s'<0} I_v(r,s').\left|n.s'\right|d\Omega' \tag{14}$$

2.3. First Law Modeling

The useful energy gained by the coolant of the FPSC is determined as [40]

$$\dot{Q}_{u,f} = \dot{m}_f c_p(T_{out} - T_{in}) \tag{15}$$

where $\dot{m}_f$ is the mass flow rate, c_p is specific heat capacity, and T_{in} and T_{out} are entering and leaving fluid temperatures.

The useful energy gained by the FPSC is determined as

$$\dot{Q}_{u,f} = A_c\left[S - U_L\left(T_{pm} - T_a\right)\right] \tag{16}$$

where A_c, T_a, and T_{pm} are respectively the absorber area, ambient temperature, and the average temperature of the absorber plate. In Equation (16), S is the absorbed solar radiation by the plate:

$$S = \eta_0 I_T \tag{17}$$

where η_0 is the optical efficiency of the FPSC:

$$\eta_0 = (\tau\alpha) = 1.01\tau\alpha \tag{18}$$

In addition, I_T can be determined as

$$I_T = I_b R_b + I_d\left[\frac{1+cos\beta}{2}\right] + I\rho_{gr}\left[\frac{1-cos\beta}{2}\right] \tag{19}$$

where I_d, I_b, and I are diffuse radiation, beam radiation, and solar radiation on the horizontal surface, respectively. In addition, R_b is the beam radiation tilt factor, which can be computed as follows:

$$R_b = \frac{cos(\varphi-\beta)\cos(\delta)cos(\omega) + sin(\varphi-\beta)sin(\delta)}{cos(\varphi)cos(\delta)cos(\omega) + sin(\varphi)sin(\delta)} \tag{20}$$

where δ is the declination angle, ω is the hour angle, and φ is latitude.

U_L is the overall heat loss coefficient, which is obtained as

$$U_L = U_t + U_b + U_e \tag{21}$$

where U_b, U_t, and U_e are the back loss coefficient, top loss coefficient, and edge loss coefficient, respectively. U_t is calculated with Equations (22)–(26) [40]:

$$U_t = \left(\frac{N}{\frac{C}{T_{pm}}\left[\frac{T_{pm}-T_a}{N+f}\right]^e} + \frac{1}{h_w}\right)^{-1} + \frac{\sigma\left(T_{pm}+T_a\right)\left(T_{pm}^2+T_a^2\right)}{\frac{1}{\varepsilon_P+.0059Nh_w} + \frac{2N+f-1+0.133\varepsilon_P}{\varepsilon_g} - N} \tag{22}$$

$$f = (1 + 0.089h_w - 0.1166h_w\varepsilon_P)(1 + 0.07866N) \tag{23}$$

$$C = 520\left(1 - 0.000051\beta^2\right) \tag{24}$$

$$e = 0.43\left(1 - \frac{100}{T_{pm}}\right) \tag{25}$$

$$h_w = 2.8 + 3V_w \tag{26}$$

where h_w and V_w are the convection coefficient of wind and wind velocity, respectively. N is the number of glass covers, and σ is the Stefan–Boltzmann constant.

In addition, U_b can be expressed as follows:

$$U_b = \frac{k}{L} \tag{27}$$

The energy efficiency of the FPSC, η, is calculated as

$$\eta = \frac{\dot{Q}_{u,f} = \dot{m}_f c_p (T_{out} - T_{in}) - P_{pump}}{I_T A_c} \tag{28}$$

where *pump* is pumping power and is defined as follows [42]:

$$P_{pump} = \frac{P_{flow}}{\eta_{pump}\eta_{motor}} \tag{29}$$

where η_{pump} and η_{motor} are the efficiency of the pump and motor, respectively. Additionally, P_{flow} is the dynamic pressure drop of the fluid and is calculated as follows:

$$P_{flow} = \frac{\dot{m}_f \Delta P}{\rho} \tag{30}$$

2.4. Second Law Modeling

Exergy is the energy that is available for use. The rate of the exergy equation is defined as follows [42]:

$$\dot{E}_{in} - \dot{E}_{out} - \dot{E}_{loss} - \dot{E}_{des} = \dot{E}_s \tag{31}$$

where $\dot{E}_S$ is the rate of storage exergy, with the assumption that the FPSC operates at a steady state equal to zero. $\dot{E}_{in}$ is the inlet exergy rate and includes the rate of inlet exergy by the inlet fluid to the FPSC ($\dot{E}in,f$) and the rate of inlet exergy of absorbed solar radiation ($\dot{E}in,Q$).

The rate of inlet exergy by the inlet fluid to the FPSC is defined as follows [36]:

$$\dot{E}_{in,f} = \dot{m}c_p\left(T_{in} - T_a - T_a ln\left(\frac{T_{in}}{T_a}\right)\right) + \frac{\dot{m}\Delta P_{in}}{\rho} \tag{32}$$

where ΔP_{in} is the difference between the pressure of the inlet fluid and ambient. The rate of inlet exergy of absorbed solar radiation is defined as follows [36]:

$$\dot{E}_{in,Q} = \eta_0 I_T A_c\left(1 - \frac{T_a}{T_s}\right) \tag{33}$$

With the assumption that the sun is a black body, T = 5777 K. According to the influence of the atmosphere on the depletion of solar radiation, *Ts* is the apparent temperature of the sun, which is about 0.75 of the sun's temperature and is approximately equal to 4333 K [43].

$\dot{E}out$ is the rate of outlet exergy and includes the rate of outlet exergy by the exiting fluid of the FPSC ($\dot{E}out,f$) [36].

$$\dot{E}_{out,f} = \dot{m}c_p\left(T_{out} - T_a - T_a ln\left(\frac{T_{out}}{T_a}\right)\right) + \frac{\dot{m}\Delta P_{out}}{\rho} \tag{34}$$

where ΔP_{out} is the difference between the pressure of the outlet fluid and ambient pressure. $\dot{E}loss$ is the rate of exhausted exergy and includes the rate of exergy exhausted from the plate to ambient ($\dot{E}i,p$) and exhausted optical exergy ($\dot{E}L$,optical).

The rate of exhausted exergy from the plate to ambient is defined [36]:

$$\dot{E}_{l,p} = U_L A_c \left(T_{pm} - T_a\right)\left(1 - \frac{T_a}{T_{pm}}\right) \tag{35}$$

Because of the optical properties of the plate, a part of the solar radiation is not absorbed. The exhausted optical exergy of the FPSC is calculated [44,45]:

$$\dot{E}_{L,optical} = \frac{(1-\eta_0)\dot{E}_{in,r}}{\dot{E}_{in,r}} = 1 - \eta_0 \tag{36}$$

$\dot{E}des$ is the rate of destroyed exergy due to temperature gradients between the plate and sun ($\dot{E}d$,ΔTp-s), temperature gradients between the plate and fluid ($\dot{E}d$,ΔTf), pressure drop from the inlet to outlet caused by the viscosity of the fluid, and the effects of walls of the heat sink ($\dot{E}d$,ΔP). These parameters are calculated as follows, respectively [36]:

$$\dot{E}_{d,\Delta T_{p-s}} = \eta_0 I_T A_c T_a \left(\frac{1}{T_p} - \frac{1}{T_s}\right) \tag{37}$$

$$\dot{E}_{d,\Delta T_{p-s}} = \dot{m} c_p T_a ln\left(\frac{T_{out}}{T_a}\right) - \dot{m} c_p T_a \frac{T_{out} - T_{in}}{T_p} \tag{38}$$

$$\dot{E}_{d,\Delta T_{p-s}} = \frac{\dot{m}\Delta p T_a ln\left(\frac{T_{out}}{T_{in}}\right)}{\rho(T_{out} - T_{in})} \tag{39}$$

The exergy efficiency of the FPSC is defined as the ratio of exergy increase of the fluid in the FPSC to the exergy of the solar radiation entering the FPSC, and it is calculated as follows [46,47]:

$$\psi = \frac{\dot{E}_{out,f} - \dot{E}_{in,f}}{I_T A_c\left(1 - \frac{T_a}{T_s}\right)} \tag{40}$$

By combining Equations (27)–(36), the exergy efficiency of water-based FPSCs equipped with elliptical tubes is achieved.

2.5. Nanofluid

The thermophysical properties of an NF are defined by the following relations [48]:

$$\rho_{nf} = (1-\varphi)\rho_f + \varphi\rho_{np} \tag{41}$$

$$\left(c_p\right)_{nf} = \frac{(1-\varphi)\left(\rho c_p\right)_f + \varphi\left(\rho c_p\right)_{np}}{\rho_{nf}} \tag{42}$$

The Patel et al. [49] model is supposed to be a general tool to predict the thermal conductivity of MWCNT-NFs. However, the model is not able to appropriately predict higher temperatures of NFs.

$$k_{nf} = k_f\left(1 + \frac{k_{np}\varphi d_f}{k_f(1-\varphi)d_{np}}\right) \tag{43}$$

The viscosity of the MWCNTs–water correlation [49,50] is defined as follows:

$$\mu_{nf} = \mu_f\left(1 - 0.50437\varphi + 1.744\varphi^2\right) \quad (44)$$

2.6. Verification and Grid Independence

A mesh study was conducted for the FPSC to evaluate the changes in the results versus grid size. As Table 3 illustrates, four sets of mesh were generated and employed to obtain the outlet temperature of the coolant. The outcomes show that a grid size of 3,728,623 nodes is suitable to perform the required simulations.

Table 3. Grid independence test.

Nodes	T_{out} (°C)	Error (%)
3,243,983	66.6782	2.22
3,599,007	70.5134	1.05
3,728,623	70.7811	0.02
3,954,131	70.7834	-

Computer software validation was performed using the method of Khorasanizadeh et al. [36]. In their study, the properties of an FPSC were evaluated by empirical measurements. Based on Figure 2, it is clear that there is a remarkable coincidence between the empirical [36] and numerical results in terms of the outlet temperature of the fluid. The maximum error between empirical and numerical results in Figure 2 is about 12.5% at 9 a.m.

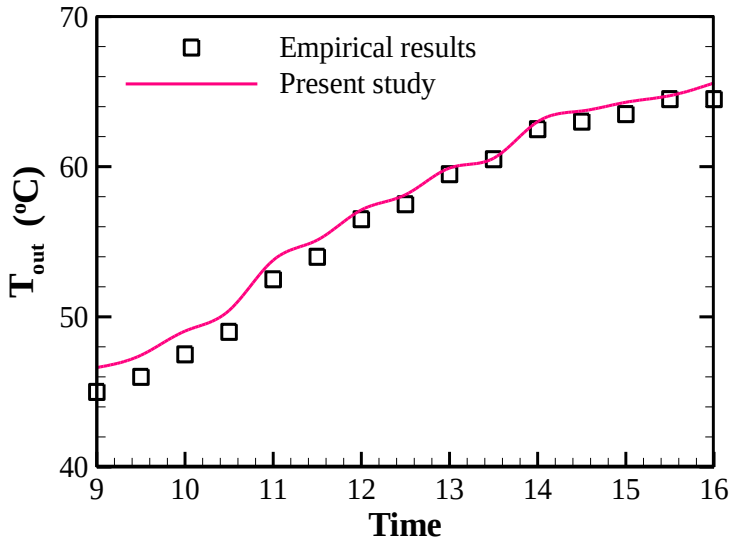

Figure 2. Comparison between the results of this study with the empirical results of Khorasanizadeh et al. [36] in terms of outlet fluid temperature.

3. Results

In this section, first, the FPSC exergy analysis is presented in two different conditions, and then the optimization case is investigated.

3.1. Energy and Exergy Analysis

The total heat loss coefficient, mean temperature of the absorber plate, FPSC outlet temperature, and energy and exergy efficiencies of a simple FPSC (with circular tubes) and of a novel FPSC equipped with elliptical tubes at different hours of the day are reported in Tables 4 and 5, respectively. All of these values are based on numerical results and analytical correlation.

Table 4. Results of reference solar FPSC.

Time	U_L (W/m^2·K)	T_{pm} (°C)	T_{out} (°C)	η (%)	ψ (%)
09:00	7.33	48.11	58.59	54.29	3.34
09:30	7.37	49.06	59.61	57.48	3.53
10:00	7.32	51.32	61.04	57.78	3.95
10:30	7.49	52.41	62.61	64.40	4.21
11:00	7.56	54.25	65.82	63.00	4.35
11:30	7.52	57.07	67.07	63.68	4.58
12:00	7.56	58.42	69.23	61.91	4.60
12:30	7.77	59.31	70.26	61.54	4.55
13:00	7.76	60.46	72.04	61.48	4.54
13:30	7.40	60.57	72.61	60.16	4.68
14:00	7.73	63.22	75.13	58.64	4.67
14:30	7.55	63.47	75.77	57.57	4.56
15:00	7.77	63.89	76.41	56.91	4.41
15:30	7.94	64.09	76.91	56.28	4.21
16:00	7.97	65.11	77.82	55.62	4.15

Table 5. Results of novel FPSC.

Time	U_L (W/m^2·K)	T_{pm} (°C)	T_{out} (°C)	η (%)	ψ (%)
09:00	7.15	47.08	53.23	64.04	6.34
09:30	7.21	48.02	54.24	67.83	6.88
10:00	7.08	50.27	55.51	68.18	7.77
10:30	7.25	51.33	57.49	75.98	8.34
11:00	7.32	53.21	59.61	74.34	8.71
11:30	7.35	56.00	62.29	76.44	9.21
12:00	7.34	57.32	63.71	74.28	9.98
12:30	7.51	58.14	64.40	73.81	8.75
13:00	7.56	59.32	65.87	73.78	8.62
13:30	7.30	59.52	66.01	72.78	8.93
14:00	7.60	62.13	68.82	69.14	8.87
14:30	7.38	62.42	68.99	69.08	8.81
15:00	7.59	62.64	69.11	66.58	8.51
15:30	7.67	63.01	69.25	65.84	8.01
16:00	7.69	64.12	69.34	65.63	7.88

It is clear that the energy and exergy efficiencies of the novel FPSC increase by about 30% and 60%, respectively, compared with the reference FPSC, owing to the more wetted surface between the plate and fluid. Furthermore, the mean temperature of the plate and the outlet temperature of the FPSC continuously increase during the day because of the FPSC inlet temperature of the fluid that is taken from the reservoir and which is constantly increasing due to FPSC performance in a closed loop and due to the heat retained in the reservoir. Furthermore, in all conditions, the inlet radiation flux rate rises from morning to midday hours and then diminishes. The energy efficiency has the same trend. However, the reason for the decreasing energy efficiency after the afternoon hours is the increasing inlet fluid temperature and also the increasing temperature of the absorber plate as time passes, which intensifies the losses.

It is clear from Tables 4 and 5 that the change in U_L in different hours is significant, so in the condition of the FPSC with a simple heat sink, the relative difference between U_L at 10:00 and that at 16:00 is about 9%. This difference is greater than that in other cases. This fact shows that the assumption of constant U_L, as some researchers have considered, is not valid [12], and it is necessary to apply its changes in measurements. Therefore, it is clear that the usage of the novel FPSC with elliptical tubes may lead to more energy and exergy efficiencies. Hence, in the next sections, the employment of an NF in a novel FPSC is analyzed.

3.2. Using a Nanofluid and Exergetic Optimization

For both conditions in which the FPSC is used, the lowest exergy and energy values are observed at 9 a.m., and both energy efficiency and exergy efficiency are dependent on the I_T and radiation angle. At 9 a.m., the I_T is less, and the angle between the direct sun radiation horizon and the vertical to the FPSC surface is high. Hence, the sun radiation absorption is less. In addition, the FPSC performance, due to the change in I_T and radiation angle, and the change in temperature of the FPSC inlet water are always transient. These conditions are of high importance in the early hours of the day and are factors that decrease efficiency. The effect of changing T_a, I_T, T_{in}, η_0, and $\dot{m}$ parameters on exergy efficiency in different φ for the optimal condition (novel FPSC) at this time was studied to optimize the FPSC from the exergy viewpoint. Therefore, when different values were considered for one parameter, the value at 9 a.m. was assigned to other parameters. The results related to the influence of changing various parameters on the exergy analysis are shown in Figures 3–7.

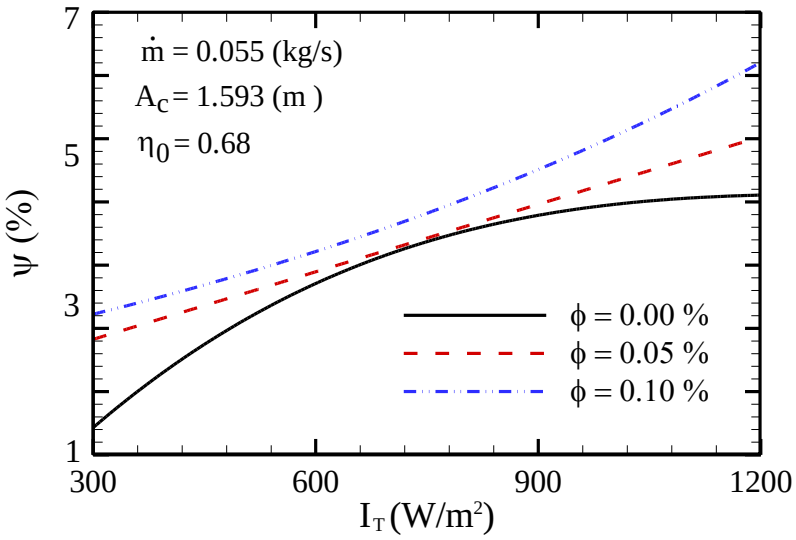

Figure 3. Variation in exergy efficiency of the novel FPSC with solar radiation in terms of ϕ.

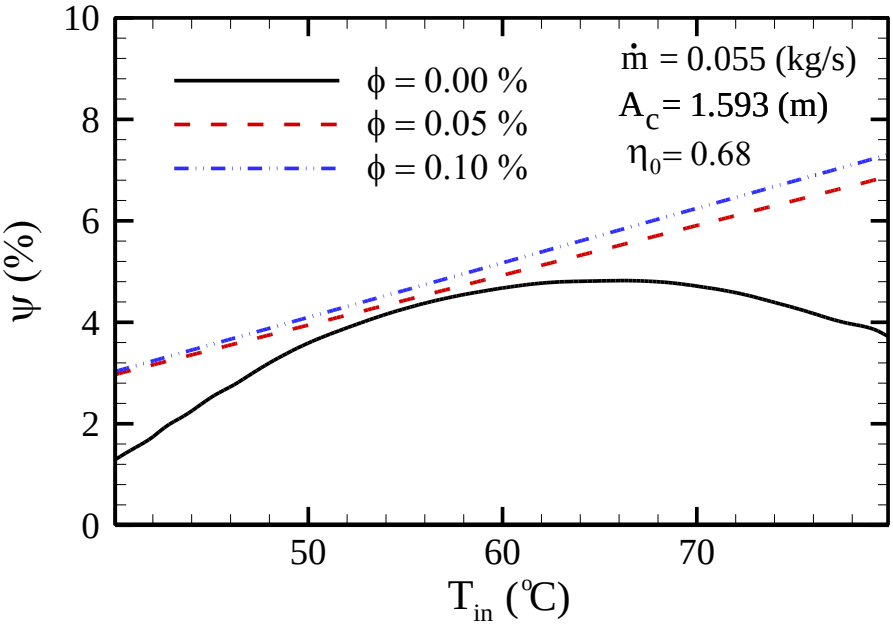

Figure 4. Variation in exergy efficiency of the novel FPSC with T_{in} in terms of φ.

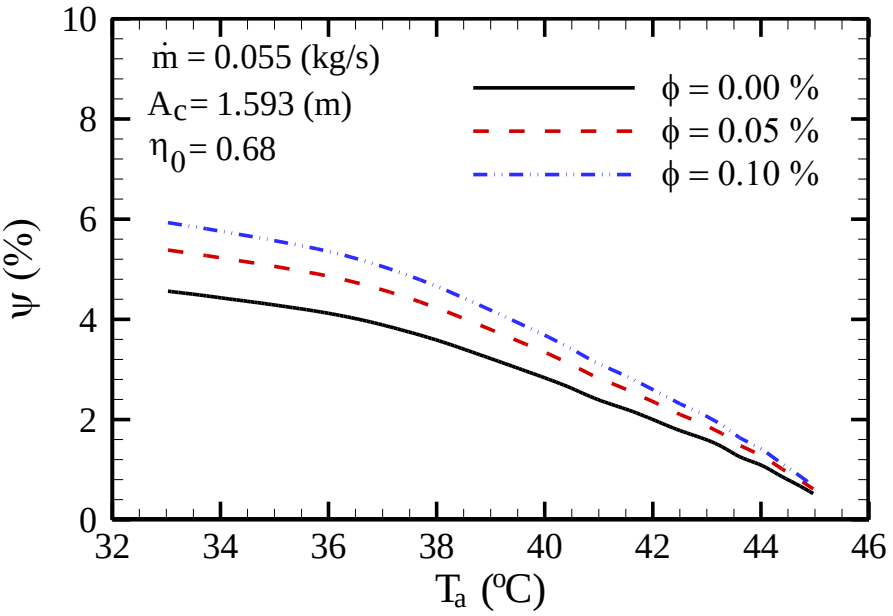

Figure 5. Variation in exergy efficiency of the novel FPSC using a nanofluid (NF) with ambient temperature in terms of φ.

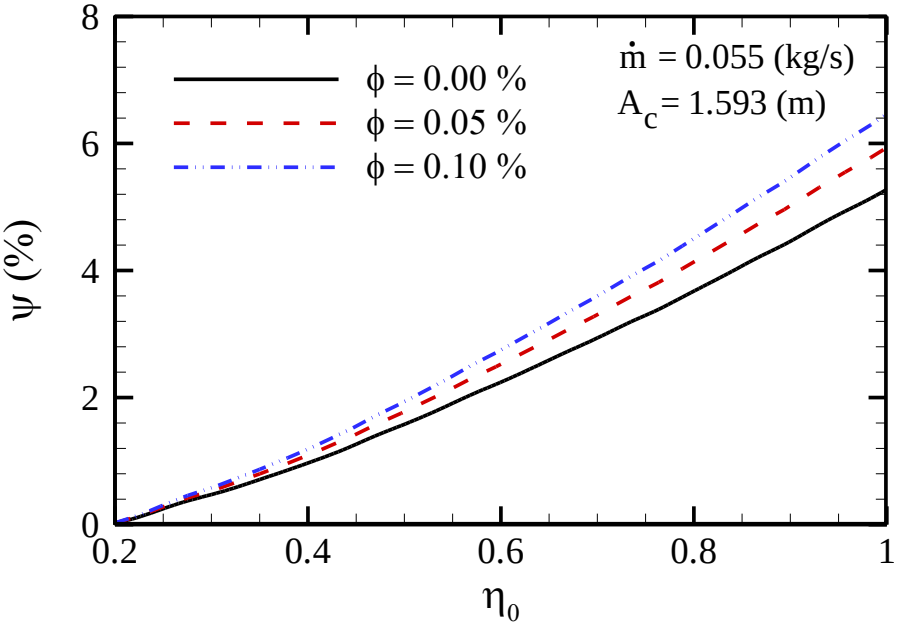

Figure 6. Variation in exergy efficiency of the novel FPSC with optical efficiency versus ϕ.

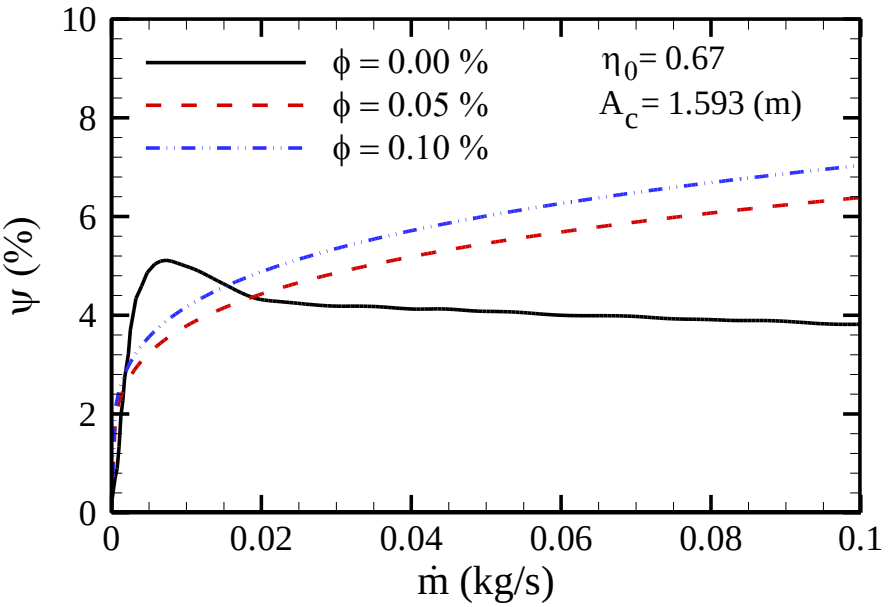

Figure 7. Variation in exergy efficiency of the novel FPSC with mass flow rate in terms of φ.

In Figure 3, the exergy efficiency variation with sun radiation flux for different ϕ is shown. In the period of changing radiation flux, from 300 to 1200 W/m^2, for all conditions, an increasing trend for the exergy value is observed. With increasing radiation of the sun, the temperature of FPSC outlet fluid rises, and this increase leads to an exergy efficiency increase. The exergy efficiency variation with FPSC inlet fluid temperature for different ϕ is demonstrated in Figure 4. For base fluid conditions, the exergy efficiency first increases until the temperature reaches 65–70 °C, and then it decreases. On the one hand, with T_{in} intensification, the outlet temperature rises, which leads to an exergy efficiency increase. On the other hand, T_{in} intensification means that the fluid temperature inside the FPSC increases, which raises the thermal loss. Therefore, there is one optimum T_{in}, and above this temperature, the effect of exergy efficiency reduction due to higher thermal loss is greater than its increase because of the increased fluid outlet temperature. However, for NF conditions, the exergy efficiency rises in response to the increased inlet temperature. The variation in exergy efficiency with ambient temperature for different ϕ is shown in Figure 5. For all three conditions, exergy efficiency decreases as ambient temperature increases. In this figure, the effect of using mixers on increasing exergy efficiency due to the heat transfer rate between the fluid and FPSC is perfectly clear. In Figure 6, the influence of increasing optical efficiency on exergy efficiency for different ϕ is demonstrated. By increasing optical efficiency for all three FPSC conditions, radiation absorption by the absorber plate is enhanced, which causes the fluid temperature inside the FPSC to rise, and therefore, the exergy efficiency rises. In Figure 7, the effect of changing the fluid mass flow rate passing through the FPSC is shown for different mass flow rates from 0.0 to 0.1 kg/s. The applied mass flow rate for three conditions was about 0.055 kg/s. From the results presented in Figure 7, it is understood that in the simulation conditions, parameters such as ambient temperature, inlet fluid temperature, optical efficiency, radiate flux, and FPSC cross-section have the same values as those in Tables 4 and 5, which are observed at 9:00 a.m. For the FPSC with the base fluid, the optimum mass flow rate that causes the maximum exergy efficiency should be 10 times lower, i.e., 0.005 kg/s. Consequently, the exergy efficiency is 5.3% instead of 4%. Nevertheless, for the condition in which the NF is used, the maximum exergy efficiency occurs with the highest mass flow rate of 0.1 kg/s.

Finally, the novel FPSC equipped with elliptical tubes and filled with the water-based NF (φ = 0.10%) is suggested as the optimum case, with maximum exergy efficiencies in almost all ranges of flow velocities in the present investigation.

Figure 8 illustrates temperature contours for the reference and novel FPSC filled with the NF at the middle plane. As observed in this figure, in the case of using elliptical tubes, the heat diffusion in the pipes is clearly increased. Furthermore, Figure 9 shows velocity contours for the reference and novel FPSC filled with the NF at the middle plane.

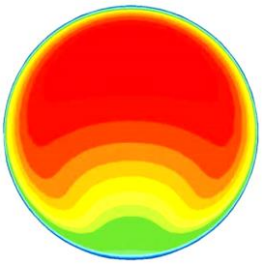

(**a**) Temperature contours for the reference FPSC at the middle plane.

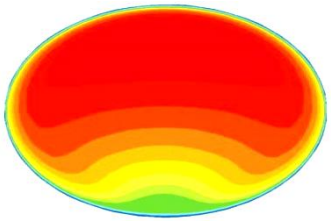

(**b**) Temperature contours for the novel FPSC at the middle plane.

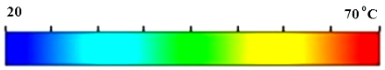

Figure 8. Temperature contours for the FPSC filled with the NF at the middle plane.

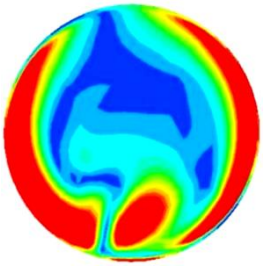

(**a**) Velocity contours for the reference FPSC at the middle plane.

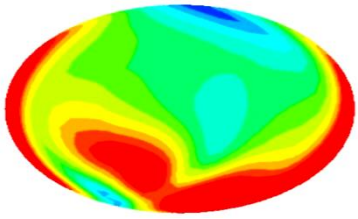

(**b**) Velocity contours for the novel FPSC at the middle plane.

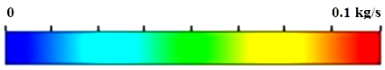

Figure 9. Velocity contours for the FPSC filled with the NF at the middle plane.

4. Conclusions

In this contribution, we studied the optimization of a novel FPSC equipped with elliptical tubes in a closed circuit for three conditions from the viewpoint of exergy analysis by assuming that U_L is the only variable parameter and that the fluid temperature is not equal to ambient temperature. The effects of using elliptical tubes instead of circular ones and of using an NF through a fluid passage were studied, and the following results were obtained:

- An increase in solar radiation flux and optical efficiency entails an exergy efficiency increase for all conditions.
- The exergy efficacy diminishes as ambient temperature increases, but by increasing the FPSC inlet fluid temperature, the exergy efficacy rises to a certain temperature and then declines.
- With the use of an NF, the exergy efficiency always intensifies with a boost of inlet temperature.
- For higher mass flow rates of the base fluid, the efficiency first slightly declines and then remains unchanged. However, by using an NF, the maximum exergy efficiency occurs with the highest mass flow rate.
- Generally, using elliptical tubes and an NF enhances the exergy efficiency. In fact, while the trend of exergy efficiency variation with effective parameters is increasing, applying the elliptical tubes causes the efficiency to increase.
- The temperature increase entails an exergy efficiency increase to a certain point, and then this efficiency is diminished for higher values.

Author Contributions: Conceptualization, S.R. and A.S.G.; methodology, M.S.; software, A.D. and A.K.H.; validation, A.K.H.; formal analysis, A.S.G.; investigation, S.R.; resources, A.K.H.; data curation, M.S.; writing—original draft preparation, S.R. and A.S.G.; writing—review and editing, S.R. and A.S.G.; visualization, A.D.; supervision, A.S.G. and M.S.S.; All authors have read and agreed to the published version of the manuscript.

Funding: This research received no external funding.

Conflicts of Interest: There is no conflict of interest.

Nomenclature

A	area (m^2)
c_p	specific heat capacity (J kg^{-1} K^{-1})
$\dot{E}$	rate of exergy (W)
h_w	wind convection coefficient (W m^{-2})
I	solar intensity (W m^{-2})
I_b	beam radiation (W m^{-2})
I_d	diffuse radiation (W m^{-2})
I_T	daily average hourly (W m^{-2})
I_v	spectral radiation intensity (W m^{-2})
K	thermal conductivity (W m^{-1} K^{-1})
M	mass flow rate (kg s^{-1})
N	number of glass covers
P	pressure (Pa)
P_{pump}	pumping power (W)
S	section of solar radiation (W m^{-2})
T	temperature (K)
T_a	ambient temperature (K)
T_{pm}	mean temperature of absorber plate
U	velocity (m s^{-1})
u'	fluctuated velocity (m s^{-1})

U	total loss coefficient (W m^{-2} K^{-1})
V_w	wind speed (m s^{-1})
Greek symbol	
α	absorption coefficient
ε	emission coefficient or dissipation
η	Efficiency
η_0	optical efficiency of collector
μ	viscosity (kg m^{-1} s^{-1})
μ_t	turbulent viscosity (kg m^{-1} s^{-1})
ρ	density (kg m^{-3})
σ	Stefan–Boltzmann constant (W m^{-2} K^{-4})
φ	latitude angle
Ω	hour angle
Subscripts	
a	ambient
c	collector
f	fluid
in	inlet
out	outlet
p	absorbent plate

References

1. Tian, M.-W.; Ebadi, A.G.; Jermsittiparsert, K.; Kadyrov, M.; Ponomarev, A.; Javanshir, N.; Nojavan, S. Risk-based stochastic scheduling of energy hub system in the presence of heating network and thermal energy management. *Appl. Therm. Eng.* **2019**, *159*, 113825. [CrossRef]
2. Tian, M.-W.; Yuen, H.-C.; Yan, S.-R.; Huang, W.-L. The multiple selections of fostering applications of hydrogen energy by integrating economic and industrial evaluation of different regions. *Int. J. Hydrog. Energy* **2019**, *44*, 29390–29398. [CrossRef]
3. Shenoy, D.V.; Shadloo, M.S.; Hadjadj, A.; Peixinho, J. Direct numerical simulations of laminar and transitional flows in diverging pipes. *Int. J. Numer. Methods Heat Fluid Flow* **2019**, *30*. [CrossRef]
4. Tian, M.-W.; Yan, S.-R.; Tian, X.-X.; Kazemi, M.; Nojavan, S.; Jermsittiparsert, K. Risk-involved stochastic scheduling of plug-in electric vehicles aggregator in day-ahead and reserve markets using downside risk constraints method. *Sustain. Cities Soc.* **2020**, *55*, 102051. [CrossRef]
5. Tian, M.-W.; Parikhani, T.; Jermsittiparsert, K.; Ashraf, M.A. Exergoeconomic optimization of a new double-flash geothermal-based combined cooling and power (CCP) system at two different cooling temperatures assisted by boosters. *J. Clean. Prod.* **2020**, *261*, 120921. [CrossRef]
6. Tian, M.-W.; Wang, L.; Yan, S.-R.; Tian, X.-X.; Liu, Z.-Q.; Rodrigues, J.J.P.C. Research on Financial Technology Innovation and Application Based on 5G Network. *IEEE Access* **2019**, *7*. [CrossRef]
7. Tian, M.; Yan, S.; Tian, X. Discrete approximate iterative method for fuzzy investment portfolio based on transaction cost threshold constraint. *Open Phys.* **2019**, *17*, 41–47. [CrossRef]
8. Li, Z.; Shahsavar, A.; Niazi, K.; Al-Rashed, A.A.A.A.; Rostami, S. Numerical assessment on the hydrothermal behavior and irreversibility of MgO-Ag/water hybrid nanofluid flow through a sinusoidal hairpin heat-exchanger. *Int. Commun. Heat Mass Transf.* **2020**, *115*, 104628. [CrossRef]
9. Pordanjani, A.H.; Aghakhani, S.; Afrand, M.; Mahmoudi, B.; Mahian, O.; Wongwises, S. An updated review on application of nanofluids in heat exchangers for saving energy. *Energy Convers. Manag.* **2019**, *198*, 111886. [CrossRef]
10. Ghalandari, M.; Maleki, A.; Haghighi, A.; Shadloo, M.S.; Nazari, M.A.; Tlili, I. Applications of nanofluids containing carbon nanotubes in solar energy systems: A review. *J. Mol. Liq.* **2020**, *313*, 113476. [CrossRef]
11. Shahsavar, A.; Khanmohammadi, S.; Afrand, M.; Shahsavar, A.; Rostami, S. On evaluation of magnetic field effect on the formation of nanoparticles clusters inside aqueous magnetite nanofluid: An experimental study and comprehensive modeling. *J. Mol. Liq.* **2020**, *312*, 113378. [CrossRef]

12. Rostami, S.; Shahsavar, A.; Kefayati, G.R.; Goldanlou, S.A. Energy and Exergy Analysis of Using Turbulator in a Parabolic Trough Solar Collector Filled with Mesoporous Silica Modified with Copper Nanoparticles Hybrid Nanofluid. *Energies* **2020**, *13*, 2946. [CrossRef]
13. Tian, Z.; Shahsavar, A.; Al-Rashed, A.A.A.A.; Rostami, S. Numerical simulation of nanofluid convective heat transfer in an oblique cavity with conductive edges equipped with a constant temperature heat source: Entropy production analysis. *Comput. Math. Appl.* **2019**, in press. [CrossRef]
14. Baniamerian, Z.; Mehdipour, R.; Kargar, F. A numerical investigation on aerodynamic coefficients of solar troughs considering terrain effects and vortex shedding. *Int. J. Eng. Trans. C Asp.* **2015**, *28*, 940–948.
15. Ziapour, B.M.; Rahimi, F. Numerical study of natural convection heat transfer in a horizontal wavy absorber solar collector based on the second law analysis. *Int. J. Eng. Trans. A Basics* **2016**, *29*, 109–117.
16. Ajay, K.; Kundan, L. Performance evaluation of nanofluid (Al_2O_3/H_2O-$C_2H_6O_2$) based parabolic solar collector using both experimental and CFD techniques. *Int. J. Eng. Trans. A Basics* **2016**, *29*, 572–580.
17. Luminosu, I.; Fara, L. Determination of the optimal operation mode of a flat solar collector by exergetic analysis and numerical simulation. *Energy* **2005**, *30*, 731–747. [CrossRef]
18. Shojaeizadeh, E.; Veysi, F. Development of a correlation for parameter controlling using exergy efficiency optimization of an Al_2O_3/water nanofluid based flat-plate solar collector. *Appl. Therm. Eng.* **2016**, *98*, 1116–1129. [CrossRef]
19. Said, Z.; Saidur, R.; Rahim, N.A. Energy and exergy analysis of a flat plate solar collector using different sizes of aluminium oxide based nanofluid. *J. Clean. Prod.* **2016**, *133*, 518–530. [CrossRef]
20. Hussein, A.K.; Kolsi, L.; Almeshaal, M.A.; Li, D.; Ali, H.M.; Ahmed, I.S. Mixed Convection in a Cubical Cavity with Active Lateral Walls and Filled with Hybrid Graphene–Platinum Nanofluid. *J. Therm. Sci. Eng. Appl.* **2019**, *11*, 041007. [CrossRef]
21. RazaShah, T.; Ali, H.M. Applications of hybrid nanofluids in solar energy, practical limitations and challenges: A critical review. *Sol. Energy* **2019**, *183*, 173–203.
22. UsmanSajid, M.; Ali, H.M. Recent advances in application of nanofluids in heat transfer devices: A critical review. *Renew. Sustain. Energy Rev.* **2019**, *103*, 556–592.
23. Ali, H.M. Recent advancements in PV cooling and efficiency enhancement integrating phase change materials based systems—A comprehensive review. *Sol. Energy* **2020**, *197*, 163–198. [CrossRef]
24. Shadloo, M.S. Numerical Simulation of Compressible Flows by Lattice Boltzmann Method. *Numer. Heat Transf. Part A* **2019**, *75*, 167–182. [CrossRef]
25. Kassem, Y.; Çamur, H.; Aateg, R.A.F. Exploring Solar and Wind Energy as a Power Generation Source for Solving the Electricity Crisis in Libya. *Energies* **2020**, *13*, 3708. [CrossRef]
26. Ahmed, S.; Muhammad Adil, H.M.; Ahmad, I.; Azeem, M.K.; e Huma, Z.; Abbas Khan, S. Supertwisting Sliding Mode Algorithm Based Nonlinear MPPT Control for a Solar PV System with Artificial Neural Networks Based Reference Generation. *Energies* **2020**, *13*, 3695. [CrossRef]
27. Lee, Y.; Kim, B.; Hwang, H. Which Institutional Conditions Lead to a Successful Local Energy Transition? Applying Fuzzy-Set Qualitative Comparative Analysis to Solar PV Cases in South Korea. *Energies* **2020**, *13*, 3696. [CrossRef]
28. Shaaban, M.F.; Alarif, A.; Mokhtar, M.; Tariq, U.; Osman, A.H.; Al-Ali, A.R. A New Data-Based Dust Estimation Unit for PV Panels. *Energies* **2020**, *13*, 3601. [CrossRef]
29. Araújo, A. Thermo-Hydraulic Performance of Solar Air Collectors with Artificially Roughened Absorbers: A Comparative Review of Semi-Empirical Models. *Energies* **2020**, *13*, 3536. [CrossRef]
30. Dijvejin, Z.A.; Ghaffarkhah, A.; Sadeghnejad, S.; Sefti, V. Effect of silica nanoparticle size on the mechanical strength and wellbore plugging performance of SPAM/chromium (III) acetate nanocomposite gels. *Polym. J.* **2019**, *51*, 693–707. [CrossRef]
31. Ghaffarkhah, A.; Afrand, M.; Talebkeikhah, M.; Sehat, A.A.; Moraveji, M.K.; Talebkeikhah, F.; Arjmand, M. On evaluation of thermophysical properties of transformer oil-based nanofluids: A comprehensive modeling and experimental study. *J. Mol. Liq.* **2020**, *300*, 112249. [CrossRef]
32. Parsa, S.M.; Davoud, J.Y.; Rahbar, A.; Majidniya, M.; Aberoumand, S.; Amidpour, Y.; Amidpour, M. Experimental assessment on passive solar distillation system on Mount Tochal at the height of 3964 m: Study at high altitude. *Desalination* **2019**, *466*, 77–88. [CrossRef]

33. Parsa, S.M.; Davoud, J.Y.; Rahbar, A.; Majidniya, M.; Aberoumand, S.; Amidpour, Y.; Amidpour, M. Experimental investigation at a summit above 13,000 ft on active solar still water purification powered by photovoltaic: A comparative study. *Desalination* **2020**, *476*, 114146. [CrossRef]
34. Parsa, S.M.; Rahbar, A.; Davoud, J.Y.; Koleini, M.H.; Afrand, M.; Amidpour, M. Energy-matrices, exergy, economic, environmental, exergoeconomic, enviroeconomic, and heat transfer (6E/HT) analysis of two passive/active solar still water desalination nearly 4000m: Altitude concept. *J. Clean. Prod.* **2020**, *261*, 121243. [CrossRef]
35. Parsa, S.M.; Rahbar, A.; Koleini, M.H.; Aberoum, S.; Afrand, M.; Amidpour, M. Desalination, A renewable energy-driven thermoelectric-utilized solar still with external condenser loaded by silver/nanofluid for simultaneously water disinfection and desalination. *Desalination* **2020**, *480*, 114354. [CrossRef]
36. Khorasanizadeh, H.; Aghaie, A. Determination of the monthly, seasonal, semi-yearly and yearly optimum tilted angles of flat plate solar collectors in Kashan. *J. Energy Eng. Manag.* **2014**, *3*, 38–49.
37. Sadeghi, R.; Shadloo, M.S.; Hooman, K. Numerical Investigation of Natural Convection Film Boiling Around Elliptical Tubes. *Numer. Heat Transf. Part A Appl.* **2016**, *70*, 707–722. [CrossRef]
38. Vanaki, S.M.; Mohammed, H.A.; Abdollahi, A.; Wahid, M.A. Effect of nanoparticle shapes on the heat transfer enhancement in a wavy channel with different phase shifts. *J. Mol. Liq.* **2014**, *196*, 32–42. [CrossRef]
39. Gray, D.D.; Giorgini, A. The validity of the Boussinesq approximation for liquids and gases. *Int. J. Heat Mass Transf.* **1976**, *19*, 545–551. [CrossRef]
40. *ANSYS Fluent-Solver Theory Guide*; Release 14.0; ANSYS Inc.: Canonsburg, PA, USA, 2011; pp. 351–353.
41. Bejan, A. *Convection Heat Transfer*; Wiley-Interscience: Hoboken, NJ, USA, 1984.
42. Duffie, J.A.; Beckman, W.A. *Solar Engineering of Thermal Processes*; John Wiley & Son: New York, NY, USA, 2006.
43. Mechanical Agitator Power Requirements for Liquid. Available online: www.pdhonline.com/courses/k103/k103content.pdf (accessed on 12 August 2020).
44. Suzuki, A. General theory of exergy balance analysis and application to solar collectors. *Energy* **1988**, *13*, 123–160. [CrossRef]
45. Bejan, A.; Keary, D.W.; Kreith, F. Second law analysis and synthesis of solar collector systems. *J. Sol. Energy Eng.* **1981**, *103*, 23–28. [CrossRef]
46. Bejan, A. *Advanced Engineering Thermo-Dynamics*; Wiley Inter science: New York, NY, USA, 1988.
47. Dutta Gupta, K.K.; Saha, S. Energy analysis of solar thermal collectors. *Renew. Energy Environ.* **1990**, *33*, 283–287.
48. Kahrobaian, A.; Malekmohammadi, H. Exergy optimization applied to linear parabolic solar collectors. *J. Fac. Eng.* **2008**, *42*, 131–144.
49. Farahat, S.; Sarhaddi, F.; Ajam, H. Exergetic Optimization of Flat Plate Solar Collectors. *Renew. Energy* **2009**, *34*, 1169–1174. [CrossRef]
50. Patel, H.E.; Anoop, K.B.; Sundararajan, T.; Das, S. Model for thermal conductivity of CNT-nanofluids. *Bull. Mater. Sci.* **2008**, *31*, 387–390. [CrossRef]